Revealing the Microscopic Mechanism of Elementary Vortex Pinning in Superconductors

C. Chen[1,10†], Y. Liu[4,8†], Y. Chen[3†], Y. N. Hu[1], T. Z. Zhang[1,11], D. Li[4,8], X. Wang[1], C. X. Wang[1], Z.Y.W. Lu[4,8], Y. H. Zhang[4,8], Q. L. Zhang[1], X. L. Dong[4,8,9], R. Wang[3,6]*, D. L. Feng[2,1,6,7]*, T. Zhang[1,5,6,7]*

[1]Department of Physics, State Key Laboratory of Surface Physics and Advanced Material Laboratory, Fudan University; Shanghai 200438, China

[2]New Cornerstone Laboratory, National Synchrotron Radiation Laboratory and School of Nuclear Science and Technology, University of Science and Technology of China; Hefei 230027, China

[3]National Laboratory of Solid State Microstructures and Department of Physics, Nanjing University; Nanjing 210093, China

[4]Beijing National Laboratory for Condensed Matter Physics, Institute of Physics, Chinese Academy of Sciences; Beijing 100190, China

[5]Hefei National Laboratory, Hefei 230088, China

[6]Collaborative Innovation Center for Advanced Microstructures; Nanjing 210093, China

[7]Shanghai Research Center for Quantum Sciences; Shanghai 201315, China

[8]School of Physical Sciences, University of Chinese Academy of Sciences; Beijing 100049, China

[9]Songshan Lake Materials Laboratory; Dongguan, Guangdong 523808, China

[10]Zhejiang Institute of Photoelectronics & Zhejiang Institute for Advanced Light Source, Zhejiang Normal University; Jinhua 321004, China.

[11]Interdisciplinary Materials Research Center, School of Materials Science and Engineering, Tongji University; Shanghai 201804, China

† These authors contributed equally.
*Corresponding authors: rwang89@nju.edu.cn, dlfeng@ustc.edu.cn, tzhang18@fudan.edu.cn

Vortex pinning is a crucial factor that determines the critical current of practical superconductors. However, the understanding of its underlying mechanism has long been phenomenological without a clear microscopic description. Here using high-resolution scanning tunneling microscopy, we studied single vortex pinning induced by point defect in layered FeSe-based superconductors. We found the defect-vortex interaction drives low-energy vortex bound states away from E_F, resulting a "mini" gap which effectively lowered the energy of vortex and caused the pinning. By measuring the local density-of-states, we directly obtained the elementary pinning energy and estimated the pinning force through the spatial gradient of pinning energy. The results align with the bulk critical current measurement. We further show that a general microscopic quantum model with considering defect-vortex interaction can well capture our observation. It indicates the local pairing near pinned vortex core is actually enhanced, which is beyond the traditional understanding that non-superconducting regions pin vortices. Our study thus revealed a general microscopic mechanism of vortex pinning in superconductors.

The ability to carry electric current without dissipation is a defining property of superconductivity. However, in practical superconductors (mostly type II superconductors), external current will apply Lorentz force on quantized magnetic flux and dissipation occurs when the accompanied vortices move (Fig. 1**a**). Fortunately, it was found that defects or disorders can prevent the motion of vortices, called flux/vortex pinning effect. The critical current density (J_C) actually depends on vortex pinning strength rather than current induced de-pairing [1, 2]. Therefore, understanding the mechanism of how a single vortex is pinned by defect, namely the elementary vortex pinning, is of fundamental importance for technological use of superconductors [3-5]. It also lays the foundation of vortex dynamics which determines the full electromagnetic response of superconductors.

In the general description, a vortex has a non-superconducting core with a size of 2ξ (ξ is the coherence length, as shown in Fig. 1**b**). Traditional understanding of vortex pinning is based on Ginzburg-Landau (G-L) theory [1,2], which consider the pinning centers as non-superconducting regions and the vortex cores attached to them will save the condensation energy cost. However, such phenomenological treatment is difficult to describe pinning centers much smaller than ξ, such as point-like defects (e.g., impurity atom or vacancy) which are the elementary form of defects in practical materials. Some theoretical works added impurity term into G-L free-energy to phenomenologically address this issue [6-8]. In fact, the microscopic description of vortex beyond the G-L theory has already been given by Caroli, de Gennes and Matricon (CdGM) [9], which predicted localized bound states with discrete energies ($E = \mu\Delta^2/E_F$, $\mu = \pm1/2, \pm3/2...$) in the vortex core (Fig. 1**b**). Meanwhile, impurity induced effect in superconductors was also extensively studied [10]. One may expect the local interaction between CdGM states and defect states shall play an important role in vortex pinning. The theoretical work by Q. Han, L.Y. Zhang and Z. D. Wang [11] has suggested such scenario. However, for a long time the study of vortex pinning has been limited to indirect transport or force measurements [1-4,12-16]. Due to the difficulty of direct investigation on the electron structure/energy of a single vortex and its pinning center (defect), the understanding of vortex pinning is still phenomenological so far.

Scanning tunnelling microscopy/spectroscopy (STM/STS) with atomic resolution is a powerful tool to study the microscopic structure of a single vortex [17]. Particularly, recent high-resolution tunneling spectrum has been able to identify discrete CdGM vortex states in various FeSe-based superconductors [18-22], as well as atomic defects induced states [23-25]. This enables direct measurement of vortex–impurity interaction in the atomic scale. In this work, we performed detailed STM study on the vortex pinning in (Li,Fe)OHFeSe and single-layer FeSe/SrTiO$_3$. We found that when a single vortex is pinned by a point defect in FeSe layer, the low-energy CdGM states are "pushed" away from E_F, which lowers the formation energy of vortices and causes the pinning. It indicates an enhanced pairing at the pinned vortex core, which is beyond the traditional understanding that it is the non-superconducting region that pins the vortex. Such novel pinning mechanism is well captured by our microscopic quantum

model describing the vortex-impurity interaction, which can be applied to general superconductors. Furthermore, via measuring the local density-of-state (DOS) distribution over the pinned/unpinned vortex cores, we are able to obtain the elementary pinning energy for the first time. We further tuned the defect-vortex distance via the repulsive vortex-vortex interaction, then the pinning force is estimated as the spatial gradient of pinning energy. The obtained value ($\sim 2\times 10^{-4}$ N/nm) aligns with the bulk critical current measurement. Our work thus sets up the microscopic mechanism of vortex pinning induced by point defect.
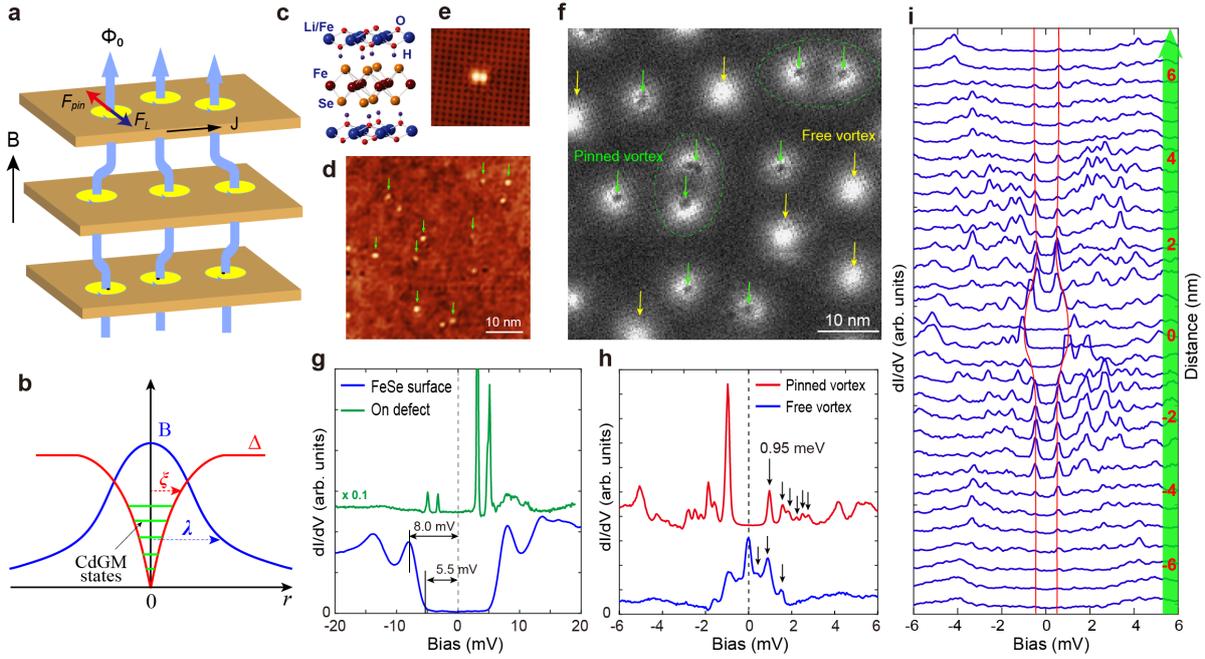
Fig. 1 | STM investigation of vortex pinning in (Li,Fe)OHFeSe. a, Illustration of vortex pinning in layered superconductor. The magnetic flux lines are pinned by individual point defects in each superconducting layer. **b**, The structure of a single vortex core. **c,** Crystal structure of (Li, Fe)OHFeSe, composed of FeSe layers and (Li,Fe)OH layers. **d**, Topographic image of the FeSe surface of (Li,Fe)OHFeSe (V_b = 50mV, I = 60pA). **e**, Atomically resolved image of a dumbbell-defect at Fe cite. **f**, Zero-bias dI/dV map at B=11T (V_b = 40mV, I = 40pA, T=4.2K), taken at the same region of panel (**d**). Green arrows in (**d**) and (**f**) indicate the positions of dumbbell defects and the pinned vortices on these defects. Yellow arrows in (**f**) indicate the free (unpinned) vortices. **g**, Typical dI/dV spectra on dumbbell-defect and defect-free region at B=0T (V_b = 20mV, I = 60pA). **h**, Typical dI/dV spectra taken at the center of pinned and free vortex cores (V_b = 17mV, I = 60pA). Arrows indicate the in-gap states. **i**, A series of dI/dV spectra taken across the pinned vortex core (V_b = 10mV, I = 60pA). The red curves track the position of the lowest CdGM states.

The STM experiment was performed in a dilution refrigerator STM (Unisoku) at the base temperature of 20 mK (T_{eff} = 160 mK) or at 4.2K when specified. The samples studied here are optimally doped (Li,Fe)OHFeSe (T_C = 42K) single crystalline film [26,27] and single-layer FeSe/SrTiO$_3$ film (sample preparation and experimental details are described in Method section). As illustrated in Fig. 1**c**, (Li,Fe)OHFeSe crystal is composed of alternatively

stacking FeSe and (Li, Fe)OH layers. We shall note that recent transport studies of (Li, Fe)OHFeSe [28] evidenced pancake-like vortices in FeSe layers (as sketched in Fig. 1**a**), and the interlayer vortex coupling is weak due to (Li, Fe)OH intercalation.

Figure 1**d** shows a topographic image of the FeSe-terminated surface of cleaved (Li, Fe)OHFeSe film. There are commonly observed "dumbbell"-shaped defects indicated by green arrows (see Fig. 1**e** for zoomed-in image), which are mostly Fe vacancies formed during sample synthesis [27]. On the defect-free region, a full superconducting gap with two pairs of coherence peaks at ±8 mV and ±14 mV is observed (Fig. 1**g**). The flat gap bottom has a half width of 5.5 meV, which corresponds to the minimum gap value. The dumbbell defects can induce pronounced impurity states (Fig. 1**g**) [25], suggesting their strong scattering potential. After applying an out-of-plane magnetic field of B=11T, vortex cores are visualized in the zero-bias conductance map shown in Fig. 1**f** (taken on the same region of Fig. 1**d**). Notably, a large portion (>50%) of vortex cores are pinned by dumbbell defects (indicated by green arrows), which makes the vortex lattice highly distorted. There are also vortices locate at defect-free region and we refer them as "free" vortices (indicated by yellow arrows). Interestingly, all the pinned vortices display a "dark spot" near their pinning site (defect site). As shown below, this feature is caused by suppressed low-energy CdGM state at defect site, which is a key manifestation of vortex pinning. Another notable feature in Fig. 1**f** is that when two pinned vortices are too close to each other (those indicated by dashed ellipses), they move slightly away from the defect sites to balance the repulsive vortex-vortex interaction and the pinning force.

Fig. 1**h** shows high-energy resolved dI/dV spectra taken at the center of pinned and free vortex cores. For free vortices, a zero-bias conductance peak (ZBCP) with a series of CdGM states around E_F are observed. The ZBCP was shown to have characteristics of Majorana zero mode [29,30]. Remarkably, in the pinned vortex the ZBCP and nearby CdGM state are absent, resulting in a "mini gap" between ±0.95 mV while a large number of discrete peaks appear outside of this gap. Fig. 1**i** shows a series of dI/dV spectra taken across a pinned vortex core. It's seen that the mini gap has the largest size at the center (defect site), but rapidly decreases to a constant value at ∼ 1.0 nm away from the pinning center. This behavior gives rise to the "dark spot" in the zero-bias dI/dV map, and evidences that the local vortex-impurity interaction drives the low-energy CdGM state away from E_F, since the distribution of impurity state is very localized (with a scale shorter than coherence length) [23-25]. The discrete peaks outside of mini gap are likely from the hybridization between CdGM state and impurity state.

A direct consequence of a mini gap opening in vortex core is that the formation energy of a pinned vortex is lowered with respected to the free vortex, as the low-energy state near gap center are reduced. This is essentially why the defect can pin the vortex. The absence of ZBCP could be due to the dumbbell defects (Fe vacancies) are strong magnetic impurities which may locally break the topological band structure of (Li,Fe)OHFeSe [20]. Meanwhile, the

dumbbell defects seen in topographic image should only pin the "pancake" vortex in the topmost FeSe layer (Fig. 1**a**), whether the vortices are affected by underneath defect is unknown (but expected to be weak). We then further examined another FeSe-based superconductor, the single-layer FeSe/SiTiO₃ which has only one FeSe layer and just show conventional CdGM in vortex cores [21, 31].
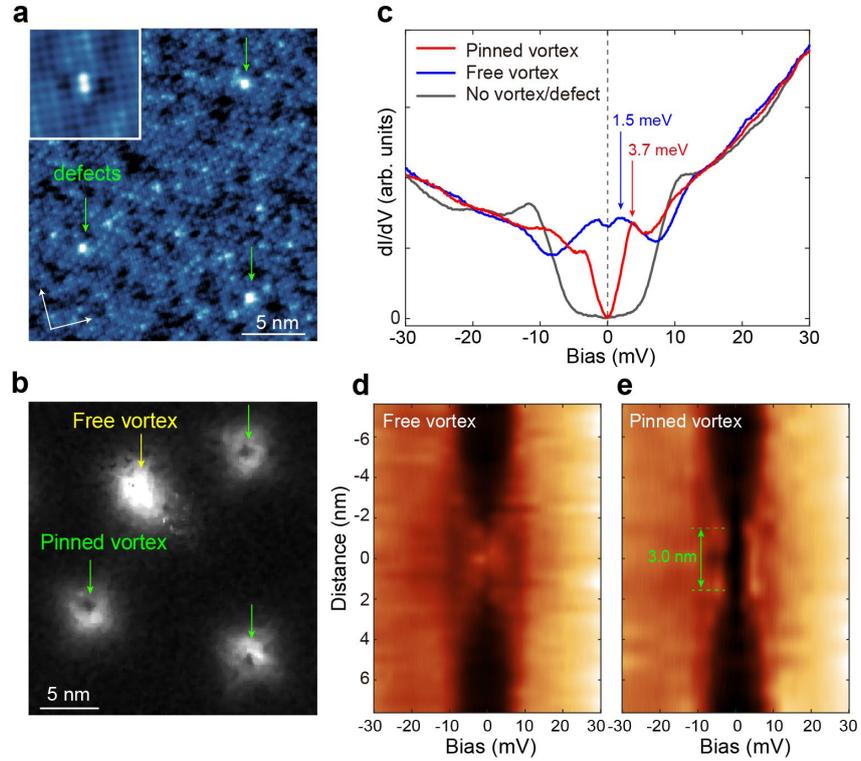
Fig. 2 | STM investigation of vortex pinning in 1ML FeSe/SrTiO₃ (001). a, Topographic image of 1ML FeSe/SrTiO₃, with green arrows indicating three "dumbbell-like" defects (V_b = 28.5mV, I = 100pA). Inset: atomically resolved image of dumbbell defect. **b**, Zero-bias dI/dV map taken at the same region of panel (**a**) under B = 8T, with green arrows indicating pinned vortices and yellow arrows indicating free vortices (setpoint: V_b = 28.5mV, I = 100pA, T = 4.2K). (**c**) dI/dV spectra measured at the center of free vortex, pinned vortex, and defect-free region at B =0T (V_b = 30mV, I = 80pA, T = 4.2K). **d,e**, Color plots of the dI/dV spectra taken across the centers of free vortex and pinned vortex, respectively (V_b = 30mV, I = 80pA, T = 4.2K).

Fig. 2**a** shows the topographic image of a single-layer FeSe/SrTiO₃. Dumbbell-like defects locate at the Fe sites are also observed, which could be Fe vacancies or impurity atoms (Fig. 2**a** inset). Fig. 2**b** shows the corresponding zero-bias dI/dV map taken under B = 8T. Clearly, there are also vortices pinned by defects, which still display "dark spot" at the defect site. In Fig. 2**c** we plot the typical dI/dV spectrum taken at the center of pinned and free vortices, and the superconducting gap at defect-free region. Although the spectra are taken at T = 4.2K, the shift of low energy CdGM states in pinned vortex is clearly seen (shifted from 1.5 mV to 3.7 mV). Figs. 2**d**, 2**e** display the color plot of dI/dV spectra taken across the free

and pinned vortices, respectively. Similar to that observed in (Li,Fe)OHFeSe, the "mini gap" is also localized around defect site within a region of ~ ±1.5 nm. Therefore, the vortex pinning behaviour in single-layer FeSe/SiTiO₃ is similar to that of (Li,Fe)OHFeSe.

A key quantity reflects the vortex pinning strength is the elementary pinning energy (U_{pin}), which is the energy difference between a pinned vortex and a free vortex. The tunneling spectra (dI/dV) directly reflect the local DOS (LDOS), thus the total energy of a vortex can be obtained by integrating LDOS over energy and the area covers the vortex core. Then the U_{pin} can be quantitively calculated via:

$$U_{pin} = \int \int_{E<-\Delta}^{E_F} N(0) \left[\left(\frac{dI}{dV} \right)_{pin} - \left(\frac{dI}{dV} \right)_{free} \right] E dE ds$$

Here the dI/dV is normalized by its value outside of superconductivity gap (normal state DOS). $N(0)$ is the absolute value of normal state DOS (per area) near E_F. The Fermi surfaces of (Li,Fe)OHFeSe of FeSe/SiTiO₃ are both composed of two electron pockets at M point [31-33], thus $N(0)$ can be obtained from the band dispersion acquired by quasi-particle interference (QPI) measurement (see Part I-1 of supplementary materials). The calculated value of U_{pin} for (Li,Fe)OHFeSe and FeSe/SrTiO₃, are -1.8 meV and -2.3 meV, respectively. To our knowledge, this is the first direct measurement of elementary pinning energy. If taking the spatial region where the mini-gap opens as the effective "pinning radius" (r_p), which is ≈1.0 nm for (Li,Fe)OHFeSe and ≈1.5 nm for 1ML FeSe/SiTiO₃, the pinning force can be estimated by $\bar{f_p} = U_{pin}/r_p$ ≈ 1.5 - 1.8×10⁻¹³N for a single pancake vortex in FeSe layer.

A more precise way to measure f_p is through the spatial gradient of U_{pin}. When a pinned vortex moves away from pinning site, $|U_{pin}|$ shall decrease and yield $f_p = \partial U_{pin}/\partial d$ (Fig. 3**a**). Here we managed to "push" a pinned vortex of (Li,Fe)OHFeSe via repulsive vortex-vortex interaction. Fig. 3**b** shows a topographic image with a few dumbbell defects (marked by numbers). Under a vertical field of B = 6T, two pinned vortices show up at defect 1 and defect cluster 3 (Fig. 3**c**). When the field increased to 7T (Fig. 3**d**), due to the rearrangement of vortex lattice, the vortex on defect cluster 3 "jumped" to defect cluster 2. Since the distance between vortex 1 and vortex 2 (10 nm) is significantly shorter than the averaged inter-vortex distance at 7T (18 nm), the repulsive interaction makes vortex 1 shift slightly with respected to its position at B = 6T. To see this spatial shift more clearly, Figs. 3**e-g** show the zoomed-in image and corresponding dI/dV maps (at E = 5 meV) around defect 1 under B = 6T, 7T, respectively. The center of the pinned vortex is determined by the ring-like high-energy CdGM state distribution in Figs. 2**f-g**. It's seen that at B = 6T there is already a small displacement between vortex center and the defect (d ≈ 0.8nm) and such displacement increased to 1.79 nm at B = 7T.

Figs. 3**h-i** show the tunneling spectra across defect 1 at B = 6T and 7T, respectively. Notably, the defect induced mini gap at B=7T is smaller than that at B = 6T (reduced from 1.9

meV to 1.1 meV), which indicates a lowered pinning energy at B = 7T. We quantitively calculate the U_{pin} difference via dI/dV maps taken over the whole vortex (see Part I-2 of supplementary materials for more details). Then the averaged pinning force in the range of 0.8nm < d <1.79 nm is obtained by: $\overline{f_p} = |\frac{U_{pin}(6T) - U_{pin}(7T)}{d_{(7T)} - d_{(6T)}}|$, which is 2.3 ×10⁻¹³ N. Considering this pinning force is applied to a single "pancake" vortex in a FeSe layer (Fig. 1a), the pinning force per unit length for bulk (Li, Fe)OHFeSe (with a c-axis constant of 0.93 nm) is $f_p' \approx 2.4 \times 10^{-4}$ N/m.
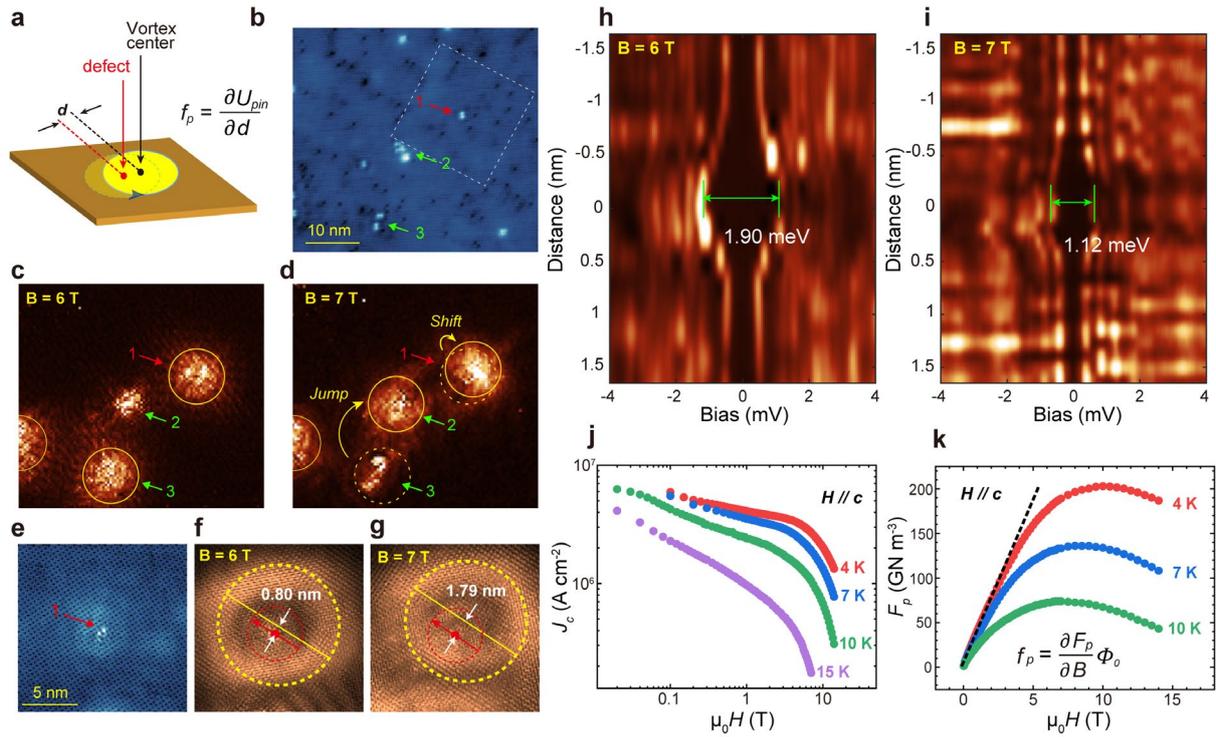
Fig. 3 | Estimation of elementary pinning force. a, Illustration of a pinned vortex with a distance of *d* away from pinning site. The pinning force is given by $f_p = \partial U_{pin}/\partial d$. **b,** Topographic image of an FeSe surface of (Li,Fe)OHFeSe, with red and green arrows indicating typical surface impurities (V_b = 100mV, *I* = 10pA). **c,d,** Zero-bias dI/dV maps under magnetic fields of 6T (panel **c**) and 7T (panel **d**) in the same region of panel (**b**). The spatial distribution of vortices varies under different magnetic fields (V_b = 30mV, *I* = 60pA, T_{eff} = 160 mK). **e,** Topographic image taken in the dashed box in panel (**b**) (V_b = 10mV, *I* = 60pA). **f,g,** dI/dV map taken at E = 5meV, under 6T and 7T in the same region of panel (**e**) (V_b = 10mV, *I* = 60pA). Yellow dashed circles track the distribution of high energy CdGM state, and red dot is the position of impurity. **h,i,** Color plots of a series of spectra taken along the positions indicated by the red arrows in panels **f** and **g**, respectively (V_b = 10mV, *I* = 60pA, T_{eff} = 160 mK). **j,k,** Magnetic field dependence of J_c at different temperatures and the corresponding pinning force density F_p. The black dashed line in (**k**) is a linear fit to the low field region.

Assuming all the vortex are pinned by the same type of dumbbell defects at low field, the bulk J_C should be determined by the (maximum) elementary pinning force via $f_p' = J_C \times \Phi_0$.

We performed J_C measurement on the (Li, Fe)OHFeSe sample. Fig. 3**j** shows the magnetic field dependence of J_C at different temperatures. At T = 4K, the variation of J_C is slow at B <5T, suggesting there are sufficient pinning sites below this vortex density. This is consistent with real-space vortex map at B =11T (Fig. 1**f**), in which over half of vortices are pinned. Fig. 3**k** shows the pinning force density ($\boldsymbol{F_p} = \boldsymbol{J_C} \times \boldsymbol{B}$) as function of B. A linear fit to the low field region (B < 2T) yields $f'_p = \frac{\partial F_p}{\partial B} \Phi_0 \approx 0.8 \times 10^{-4}$ N/m. Comparing to the traditional strong pinning theory [2] which gives $f'_p = 0.45\pi\xi\mu_0 H_c^2 = 0.45 \frac{\Phi_0^2}{8\pi\xi\lambda^2\mu_0} \approx 8.0 \times 10^{-4}$ N/m (taken ξ = 2.6 nm and λ = 160 nm for (Li, Fe)OHFeSe film [35]), our microscopic measurement based on tunneling spectrum already gives a reasonable estimation on f'_p. The relatively large value of elementary pinning force with comparing to bulk J_c could be due to that there still exists interlayer coupling between the pancake vortices in (Li,Fe)OHFeSe (Fig. 1**a**). Since the defects are randomly distributed, the pinning forces applied on pancake vortices in neighboring FeSe layers may be partially canceled if the vortex cores are not aligned vertically (flux line rigidity induced summation problem [1,2]).

So far, we have directly detected vortex-defect interaction which shifts CdGM states and show that it is responsible for vortex pinning. The mini-gap opening at pinned vortex core (Figs. 1**i** and 2**e**) intuitively indicates a locally enhanced pairing. This is rather beyond the phenomenological description that a non-superconducting region pins the vortex [1,2]. To elucidate the underlying mechanism, we carried out microscopic model calculations. The system consists of a conventional superconductor with a vortex and a defect (both located at $\boldsymbol{r} = 0$). The superconducting state is described by the mean-field Hamiltonian $H_{SC} = \sum_\sigma \int d\boldsymbol{r}[(-\hbar^2\nabla^2/2m - \mu)c_{r\sigma}^\dagger c_{r\sigma} + \Delta(\boldsymbol{r})c_{r\sigma}^\dagger c_{r\bar\sigma}^\dagger + \Delta^*(\boldsymbol{r})c_{r\bar\sigma}c_{r\sigma}]$. The local pairing potential is given by $\Delta(\boldsymbol{r}) = \Delta(r)e^{iv\theta}$, where θ is the angle of $\boldsymbol{r}$, and $v = 1$ characterizes the SC phase winding. The local gap function takes the form $\Delta(r) = \Delta_0 r/\sqrt{r^2 + \xi^2}$ [36]. Δ_0 is the pairing potential far away from the vortex core and ξ is the local coherent length. The defect can be described by $H_{imp} = \sum_\sigma \varepsilon_d d_\sigma^\dagger d_\sigma$, where ε_d is the impurity level and $d_\sigma^\dagger(d_\sigma)$ is the creation (annihilation) operator of the local impurity state. The hybridization between the impurity and the electrons of superconducting state is given by $H_{hyb} = \sum_\sigma \int d\boldsymbol{r}[V_0(r)d_\sigma^\dagger c_{r\sigma} + h.c.]$, where the coupling decays with the distance, $V_0(\boldsymbol{r}) = V_0 e^{-(r/r_0)^2}/\sqrt{\pi}r_0$ with r_0 being the decay length [37]. The above model $H_{SC} + H_{imp} + H_{hyb}$ constitutes a microscopic continuum description of the experimental system (see more details in Part II of supplementary materials), which better captures the low-temperature physics at thermodynamic limit compared to the phenomenological Ginzberg-Landau theory [1,2].

The corresponding Bogoliubov-de-Genne equation can be most naturally written in a basis expanded by the orbital angular momentum (OAM) partial waves and the Bessel functions. For $V_0 = 0$, the impurity is uncoupled to the SC. We calculate the in-gap spectrum that shown in Fig. 4a. A series of in-gap CdGM states characterized by different OAMs take place. For $V_0 \neq 0$, the coupling term relevant to the in-gap physics can be readily derived from H_{hyb} after the Bogoliubov transformation, i.e.

$$H_{\text{imp-CdGM}} = 2\pi \sum_\sigma \int dr r V_0(r)[u(r)d_\sigma^\dagger \gamma_{-1/2} + v^*(r)\gamma_{1/2}^\dagger d_\sigma] + h.c. \qquad (1)$$

where $u(r)$, $v(r)$ are factors associated with the transformation. $\gamma_{\pm 1/2}$ denotes the Bogoliubov quasi-particle operator corresponding to the two lowest CdGM states with OAM $m = \pm 1/2$, as marked by red in Fig. 4a. Eq. (1) indicates that the major effect of the impurity is to couple with the lowest two CdGM states, as schematically depicted by Fig. 4b. This impurity-CdGM coupling is the driving force for the shift of the CdGM states.
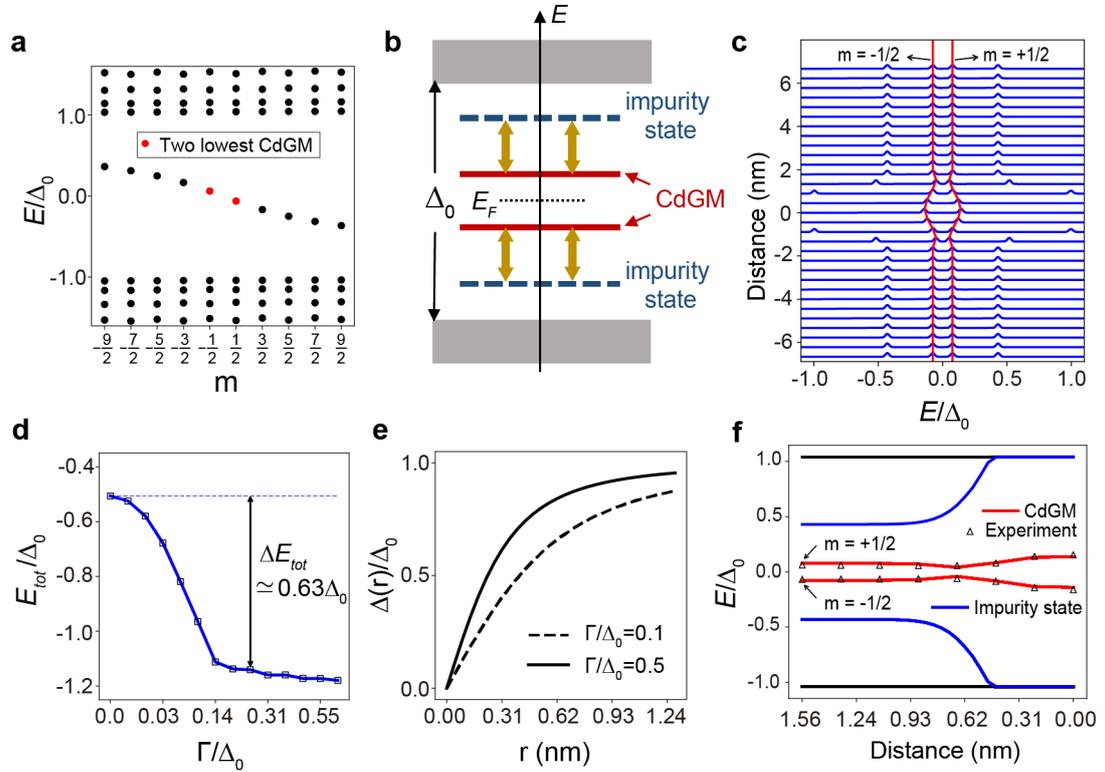
Fig. 4 | Microscopic modeling of vortex pinning. a, The calculated energy spectrum for the free vortex case. Two lowest CdGM states with OAM $m = \pm 1/2$ are marked by red. **b**, The microscopic mechanism driving the shift of CdGM states. The impurity is strongly coupled to the lowest CdGM with OAM $m = \pm 1/2$, while leaves the other CdGM states nearly unchanged. **c**, The evolution of the in-gap LDOS with varying d firstly towards and then away from the vortex core. The red curve highlights the evolution of CdGM states. The two higher energy peaks are contributed by the impurity states. **d**, The total energy of the lowest CdGM states and the impurity state as a function of Γ. **e**, The local gap function, $\Delta(r)$, self-consistently determined for different Γ. **f**, The zoom-in data in the region near the vortex core, which makes a closer comparison between the numerical results and the experiments. To better describe experiments where the dumbbell defect has a p-wave anisotropy, we

added a small anisotropic scattering term of the strength V_1 (See Part II of supplementary materials). This term is not necessary for the general pinning mechanism and does not affect ΔE_{tot} obtained in panel (**d**), although it leads to a better quantitative agreement with experiments in Fig. 1(**i**). The parameters used in the calculations are: Δ_0=5.5meV, $\varepsilon_d = 2.4$meV, $\mu = 110$meV, $V_1 = 5.5$meV, $r_0 = 0.53$nm.

The hybridization $V_0(d)$ between the impurity and the local electrons decays with the distance to impurity (d). We calculate the evolution of the lowest CdGM states and the impurity state with changing d. As shown in Fig. 4**c**, with lowering d, the in-gap states firstly stay intact. However, when getting close to the vortex core ($d \lesssim 2$nm), due to the enhanced impurity coupling, the two lowest CdGM states are pushed towards slightly and then away from the Fermi energy E_F (see part II-2 of supplementary materials for details). The zoom-in figure in Fig. 4**f** clearly shows a significant energy shift of the lowest CdGM states, which saturates to higher energies away from E_F at $d = 0$. The results are in quantitative agreement with the experimental data extracted from Fig. 1**i**. We also found that, accompanied by the shift of the CdGM states, the local pairing around the vortex core is simultaneously enhanced, as shown by Fig. 4**e**. This is reflected by reduced coherence length in the vortex core with an impurity, obtained by the self-consistent calculation of gap equation (see Part II-3 of supplementary materials).

The shift of the in-gap states inevitably modifies the energetics of the superconducting system. We then calculate and plot the total energy of the lowest CdGM states and the impurity state (below E_F), E_{tot}, as a function of the broadening function $\Gamma = \pi \rho_0 V_0^2$ with ρ_0 the DOS of the normal state. Since all the other CdGM states ($m \neq \pm 1/2$) and the above-gap continuum are barely affected by the impurity, the quantity $\Delta E_{tot} = E_{\text{tot}}(V_0) - E_{\text{tot}}(0)$ (for large V_0), is essentially the energy difference between a pinned vortex and a free vortex. Thus, ΔE_{tot} offers the magnitude of elementary pinning energy U_{pin} in the perspective of a microscopic description. ΔE_{tot} is evaluated around $-0.63\Delta_0$ in Fig. 4**d**, i.e., -3.47 meV for $\Delta_0 \sim 5.5$meV (see Fig. 1**g**), which is of comparable value with the U_{pin} estimated by experiments.

Therefore, our microscopic model well accounts for the experimental findings above. We note the CdGM-impurity coupling revealed in Eq. (1) is a general result. Its existence neither relies on the pairing details nor the type of impurity, i.e., magnetic or non-magnetic. Although non-magnetic impurity does not affect the bulk property of isotropic s-wave superconductors, its effect is non-negligible when a vortex is in presence. Since the vortex locally breaks time-reversal symmetry (TRS), the impurity-pinned vortex also violates TRS, and consequently shares common properties with a magnetic impurity. This will inevitably lead to significant modifications to the in-gap physics of s-wave superconductors. Microscopically, non-magnetic impurity can induce impurity bound states near the gap edge [10]. These impurity states are coupled to the lowest CdGM states, generating the pinning effect

according to our calculations. In previous phenomenological pinning theory [1], pair breaking/non-breaking impurities are believed to affect the coefficient of different terms of G-L free-energy (so called δT_C and δl pinning). Here, we reveal that their microscopic pinning mechanism could be unified by the impurity-CdGM coupling. In addition, Fig. **4d** shows that the impurity coupling strength V_0 is the key factor that determines the pinning energy and thus the pinning force. This observation would provide a guidance for the search of superconductors with large critical current J_C.

In summary, we have performed a comprehensive study on the elementary vortex pinning in FeSe-based superconductors. High-resolution tunneling spectrum reveals that the coupling between vortex and impurity state is the origin of vortex pinning. The elementary pinning energy/force are extracted from local tunneling spectra, which set up a direct connection between the microscopic electronic structure of vortex and the macroscopic transport quantity of J_C for the first time. The pinning mechanism is well captured by our quantum impurity model in an s-wave superconductor with a vortex. The obtained results are not sensitive to the detailed features of the pairing and impurity, thus are applicable to broad classes of superconductors and pinning centers. Therefore, our study reveals a general microscopic mechanism of vortex pinning, which enables practical superconductors to carry non-dissipative current.

References:
1. G. Blatter, M. V. Feigel'man, V. B. Geshkenbein, et al. Vortices in high-temperature superconductors. *Rev. Mod. Phys.* **66**, 1125 (1994).
2. T. Matsushita, Flux pinning in superconductors. Springer Berlin Heidelberg (2007).
3. W. K. Kwok, U. Welp, A. Glatz, et al. Vortices in high-performance high-temperature superconductors. *Reports on Progress in Physics* **79**, 116501 (2016).
4. S. Eley, A. Glatz, R. Willa, Challenges and transformative opportunities in superconductor vortex physics. *Journal of Applied Physics* **130** (5) (2021).
5. D. Larbalestier, A. Gurevich, D. M. Feldmann, A. Polyanskii, High-Tc superconducting materials for electric power applications. *Nature* **414**, 368–377 (2001).
6. E. V. Thuneberg, J. Kurkijärvi, D. Rainer, Pinning of a Vortex Line to a Small Defect in Superconductors. *Phys. Rev. Lett.* **48**, 1853 (1982).
7. E. V. Thuneberg, J. Kurkijärvi, D. Rainer, Elementary-flux-pinning potential in type-II superconductors. *Phys. Rev. B* **29**, 3913 (1984).
8. M. Friesen, P. Muzikar, Microscopic theory of vortex pinning: Impurity terms in the Ginzburg-Landau free energy. *Phys. Rev. B* **53**, R11953 (1996).
9. C. Caroli, P. D. Gennes, J. Matricon, Bound Fermion states on a vortex line in a type II superconductor. *Phys. Lett.* **9**, 307 (1964).
10. A. V. Balatsky, I. Vekhter, J. X. Zhu, Impurity-induced states in conventional and unconventional superconductors. *Rev. Mod. Phys.* **78**, 373 (2006).
11. Q. Han, L. Zhang, Z. D. Wang, Effect of a point impurity on the vortex bound states in an s-wave superconductor: a self-consistent analysis. *Phys. Rev. B* **62**, 5936 (2000).

12. O. B. Hyun, D. K. Finnemore, L. Schwartzkopf, et al. Elementary pinning force for a superconducting vortex. *Phys. Rev. Lett.* **58**, 599 (1987).

13. J. Mannhart, J. Bosch, R. Gross, et al. Elementary pinning forces measured using low temperature scanning electron microscopy. *Physics Letters A* **122** (8), 439-442 (1987).

14. L. H. Allen, J. H. Claassen, Technique for measuring the elementary pinning force in thin films. Phys. Rev. B **39** (4), 2054 (1989).

15. O. M. Auslaender, L. Luan, E. W. J. Straver, et al. Mechanics of individual isolated vortices in a cuprate superconductor. *Nat. Phys.* **5** (1), 35-39 (2009).

16. L. Embon, Y. Anahory, A. Suhov, et al. Probing dynamics and pinning of single vortices in superconductors at nanometer scales. *Sci. Rep.* **5** (1), 7598 (2015).

17. H. Suderow, I. Guillamón, J. G. Rodrigo, S. Vieira, Imaging superconducting vortex cores and lattices with a scanning tunneling microscope. *Supercond. Sci. Technol.* **27**, 063001 (2014).

18. M. Y. Chen, X. Chen, H. Yang, Z. Du, X. Zhu, E. Wang, and H. H. Wen, Discrete energy levels of Caroli–de Gennes–Matricon states in quantum limit in $FeTe_{0.55}Se_{0.45}$. *Nat. Commun.* **9**, 970 (2018).

19. Q. Liu, et al. Robust and clean Majorana zero mode in the vortex core of high-temperature superconductor $(Li_{0.84}Fe_{0.16})OHFeSe$. *Phys. Rev. X* **8**, 041056 (2018).

20. L. Y. Kong, et al. Half-integer level shift of vortex bound states in an iron-based superconductor. *Nat. Phys.* **15**, 1181 (2019).

21. C. Chen et al. Observation of discrete conventional Caroli-de Gennes-Matricon states in the vortex core of single-layer $FeSe/SrTiO_3$. *Phys. Rev. Lett.* **124**, 097001 (2020).

22. T. Z. Zhang, et al. Observation of distinct spatial distributions of the zero and nonzero energy vortex modes in $(Li_{0.84}Fe_{0.16})OHFeSe$. *Phys. Rev. Lett.* **126**, 127001 (2021).

23. A. Yazdani, B. A. Jones, C. P. Lutz, M. F. Crommie, and D. M. Eigler, Probing the local effects of magnetic impurities on superconductivity. *Science* **275**, 1767 (1997).

24. S.-H. Ji, et al. High-Resolution Scanning Tunneling Spectroscopy of Magnetic Impurity Induced Bound States in the Superconducting Gap of Pb Thin Films. *Phys. Rev. Lett.* **100**, 226801 (2008).

25. T. Z. Zhang et al. Phase shift and magnetic anisotropy induced field splitting of impurity states in $(Li_{1-x}Fe_x)OHFeSe$ superconductor. *Phys. Rev. Lett.* **130**, 206001 (2023).

26. Y. L. Huang et al. Superconducting (Li,Fe)OHFeSe film of high quality and high critical parameter. *Chin. Phys. Lett.* **34**, 077404 (2017).

27. X. Dong, F. Zhou and Z. Zhao, Electronic and Superconducting Properties of Some FeSe-Based Single Crystals and Films Grown Hydrothermally. *Front. Phys.* **8**, 586182 (2020)

28. D. Li, et al. Quasi-Two-Dimensional Nature of High-Tc Superconductivity in Iron-Based (Li, Fe)OHFeSe. *Chin. Phys. Lett.* **39**, 127402 (2022).

29. C. Chen, et al. Quantized conductance of Majorana zero mode in the vortex of the topological superconductor $(Li_{0.84}Fe_{0.16})OHFeSe$. *Chin. Phys. Lett.* **36**, 057403 (2019).

30. X. Wang et al., STM study on the vortex states and Majorana zero-modes in FeSe-based high-Tc superconductors. *Quantum Frontiers*, **1**, 12 (2022)

31. Q. Fan, et al., Plain s-wave superconductivity in single-layer FeSe on $SrTiO_3$ probed by scanning tunneling microscopy. *Nat. Phys.* **11**, 946 (2015).

32. S. Y. Tan, et al., Interface-induced superconductivity and strain-dependent spin density waves in FeSe/SrTiO3 thin films. *Nat. Mater.* **12**, 634 (2013).

33. L. Zhao, A. Liang, D. Yuan, et al. Common electronic origin of superconductivity in (Li, Fe)OHFeSe bulk superconductor and single-layer $FeSe/SrTiO_3$ films. *Nat. Commun.* **7**, 10608

(2016).

34. X. H. Niu, R. Peng, H. C. Xu, et al. Surface electronic structure and isotropic superconducting gap in (Li$_{0.8}$Fe$_{0.2}$)OHFeSe. *Phys. Rev. B* **92**, 060504 (2015).

35. J. Hänisch, et al. Anisotropy of flux pinning properties in superconducting (Li, Fe) OHFeSe thin film. *Supercond. Sci. Technol.* **33**, 114009 (2020).

36. I. M. Khaymovich, N. B. Kopnin, A. S. Mel'nikov, I. A. Shereshevskii, Vortex core states in superconducting graphene. *Phys. Rev. B* **79**, 224506 (2009).

37. B. S. de Mendonça, A. L. R. Manesco, N. Sandler, L. G. G. V. Dias da Silva, Near zero energy Caroli–de Gennes–Matricon vortex states in the presence of impurities. *Phys. Rev. B* **107**, 184509 (2023).

Methods:

Sample preparation: High quality (Li$_{0.8}$Fe$_{0.2}$)OHFeSe single crystalline films were grown on LaAlO$_3$ substrate by matrix-assisted hydrothermal epitaxy, as described in Refs. [26,27]. The sample was cleaved in ultra-high vacuum and transferred to STM head right after cleaving. 1ML FeSe/ SrTiO$_3$ sample was grown by co-deposition of high purity Se (99.999%) and Fe (99.995%) on SrTiO$_3$ (001) substrate holding at 670 K, followed by annealing at ~800 K for 1 hours. The SrTiO$_3$ (001) (0.5% Nb doping) substrate were cleaned by direct heating at 1250K in ultra-high vacuum.

STM measurement: The STM experiment was performed in a dilution refrigerator STM (Unisoku) at the base temperature of 20 mK (T$_{eff}$ = 160 mK) or at 4.2K when specified. Normal PtIr tips were used and cleaned by e-beam heating. Topographic images are taken with constant current mode with bias voltage (V_b) applied to the sample. The tunneling conductance *dI/dV* is collected by standard lock-in method with a modulation frequency of 973 Hz. The typical modulation amplitude (ΔV) is 30 μeV at T = 20mK and 0.2 meV at T=4.2K.

Transport measurement of J$_C$: Transport measurements under magnetic field up to B = 14 T were carried out via standard four-probe method in a Quantum Design PPMS DynaCool system. The values of J$_C$ were obtained using the criteria of 1 μV on I–V curves and the bridge parameters were characterized by a Bruker DektakXT stylus profilometer.

Solving the Bogoliubov-de-Genne (BdG) equation of SCs with a pinned vortex: Three steps of transformation are performed to cast the BdG Hamiltonian in a proper matrix form. We first make a gauge transformation that removes the phase winding of the pairing potential. Then, we expand the wave function in terms of the partial waves of different OAMs, denoted by m. Finally, the radial dependence of the wave function is expanded in the complete basis formed by Bessel functions. For each m, the final BdG Hamiltonian is written into a $4N + 4$ dimensional matrix, where the $4N$ comes from tensor product of the Nambu, spin and the Bessel function space. N is the cutoff in terms of the number of Bessel functions used in the expansion, and $N = 100$ is used in the calculations, which is large enough to ensure numerical convergence. The additional 4 dimension of the matrix comes from the impurity Hilbert space, which consists of the empty, doubly-occupied state, and two singly-occupied states. Exact diagonalization then generates a complete and accurate spectrum of the experimental system,

including the CdGM, the impurity state, and the above-gap continuum. More details are included in Part II of the supplemental materials.

Author contributions:

The STM measurements and data analysis were performed by C. Chen, T. Z. Zhang, Y. N. Hu and T. Zhang. (Li,Fe)OHFeSe sample preparation and J_C measurement were performed Y. Liu, D. Li, Z.Y.W. Lu, Y.H. Zhang and X. L. Dong. Model calculation was performed by Y. Chen and R. Wang. D. L. Feng and T. Zhang coordinated the project. C. Chen, R. Wang and T. Zhang wrote the manuscript. All authors have discussed the results and the interpretation.

Competing interests: Authors declare that they have no competing interests.

Data and materials availability:
All data are available in the main text or the supplementary materials.

Supplementary Materials for
Revealing the Microscopic Mechanism of Elementary Vortex Pinning in Superconductors

C. Chen[†], Y. Liu[†], Y. Chen[†], Y. N. Hu, T. Z. Zhang, D. Li, X. Wang, C. X. Wang, Z.Y.W. Lu, Y. H. Zhang, Q. L. Zhang, X. L. Dong, R. Wang*, D. L. Feng*, T. Zhang*

†These authors contributed equally.
*Corresponding authors: rwang89@nju.edu.cn, dlfeng@ustc.edu.cn, tzhang18@fudan.edu.cn

Part I: Obtaining the elementary pinning energy/force

I -1. Calculation of elementary pinning energy through linecut tunneling spectra

In STM measurement, the tunneling conductance (dI/dV) at a bias voltage of V is proportional to the local density-of-state (LDOS) of the sample, assuming the tip DOS and tunneling matrix element are constants near E_F:

$$\frac{\mathrm{d}I}{\mathrm{d}V}(V, \boldsymbol{r}) \propto \rho_s(E_F + eV, \boldsymbol{r})$$

In a superconducting state, the energy gap opening in single-particle DOS lowers the free-energy of the system, which contributes to the main part of condensation energy. Any in-gap bound state (like the CdGM state) will reduce the condensation energy and be destructive to superconductivity. Via integrating the LDOS over an energy range covers superconducting gap and an area covers the whole pinned/free vortex core, we can obtain the condensation energy diffidence between a pinned and a free vortex core, which is defined as the elementary pinning energy U_{pin}. The absolute value of LDOS can be obtained by calibrating the dI/dV spectra with the normal state DOS near E_F of the host superconductor. Then U_{pin} is expressed as:

$$U_{pin} = \int \int_{E<-\Delta}^{E_F} N(0) \left[\left(\frac{\mathrm{d}I}{\mathrm{d}V}\right)_{\text{pinned}} - \left(\frac{\mathrm{d}I}{\mathrm{d}V}\right)_{\text{free}} \right] E \mathrm{d}E \mathrm{d}s$$

Here the dI/dV is normalized by its value outside of superconducting gap, as shown in Figs. S1(c,f) for examples (which are normalized at E = -17 meV). $N(0)$ is the normal state DOS near E_F (per area). For (Li,Fe)OHFeSe and 1 ML FeSe/SrTiO$_3$ superconductors, their Fermi surfaces (contributed by a single FeSe layer) are composed of *two* near circular electron pockets at the M point (refs. *32-34*), as sketched in Fig. S2(a). $N(0)$ can be extracted from the band dispersion of these pockets measured by *in-situ* quasi-particle interference (QPI) shown Fig. S2. Here we used a parabolic curve $E(q) = aq^2 - E_b$ ($q = 2k$) to fit the dispersion in Fig. S2(d,e). which yield E_b = 50meV, k_F = 0.17Å^{-1} for (Li,Fe)OHFeSe, and E_b = 60meV, k_F = 0.20 Å^{-1} for 1ML FeSe/SrTiO$_3$. Then $N(0) = 2S \cdot 2\pi k dk / 4\pi^2 dE = 2S k_F^2 / 4\pi E_b$ (S=2 is the spin degeneracy).

For free vortex and a pinned vortex with a defect at its center, their CdGM states all have near isotopic distribution. Then the spatial integration of LDOS can be obtained through a linecut dI/dV spectra taken across the vortex core (as shown in Fig. S1(a,b,d,e)), via:

$\int(\frac{dI}{dV})_{(r)}2\pi r dr$. All the integrations were performed numerically with a spatial resolution <0.5 nm and an energy resolution <0.1 meV. The calculated value of U_{pin} is -1.8 meV for (Li,Fe)OHFeSe and -2.3 meV for 1 ML FeSe/SrTiO$_3$.
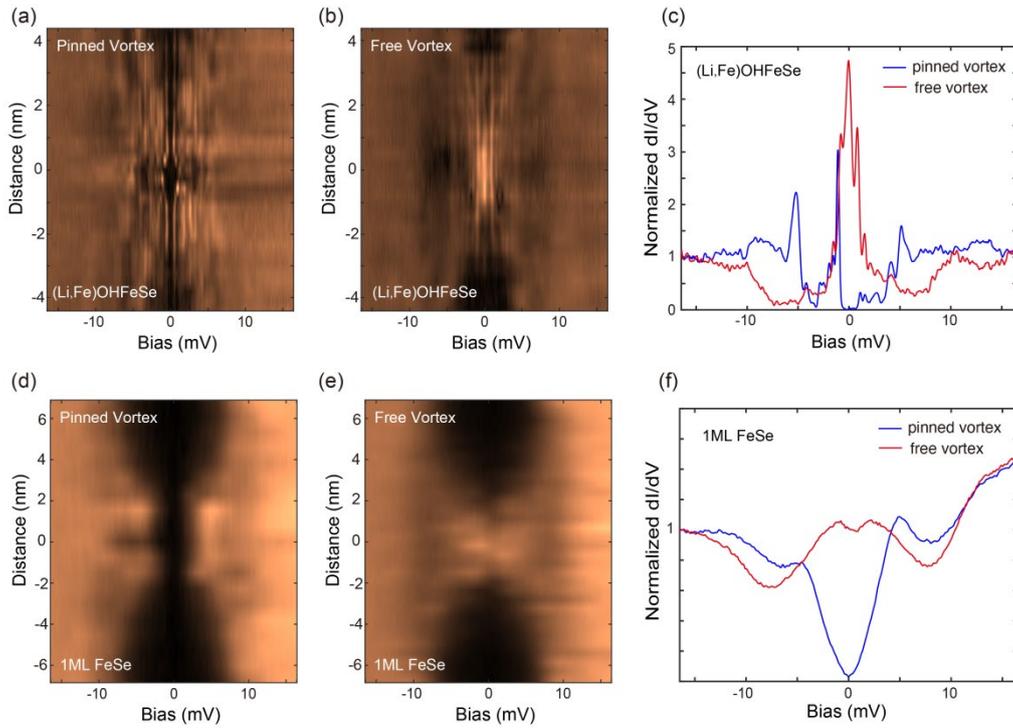
Fig. S1 (**a,b**) Color plots of linecut dI/dV spectra taken across the center of pinned vortex and free vortex in (Li,FeOH)FeSe. (V_b = 17mV, I = 60pA, T_{eff} = 160mK) (**c**) Normalized dI/dV spectra taken at the center of pinned and free vortex cores of (Li,Fe)OHFeSe. (**d, e**) Color plots of linecut dI/dV spectra taken across the center of pinned vortex and free vortex in 1ML FeSe/SrTiO$_3$ (V_b = 30mV, I = 80pA, T = 4.2K). (**f**) Normalized dI/dV spectra taken at the center of pinned and free vortex cores of 1ML FeSe.
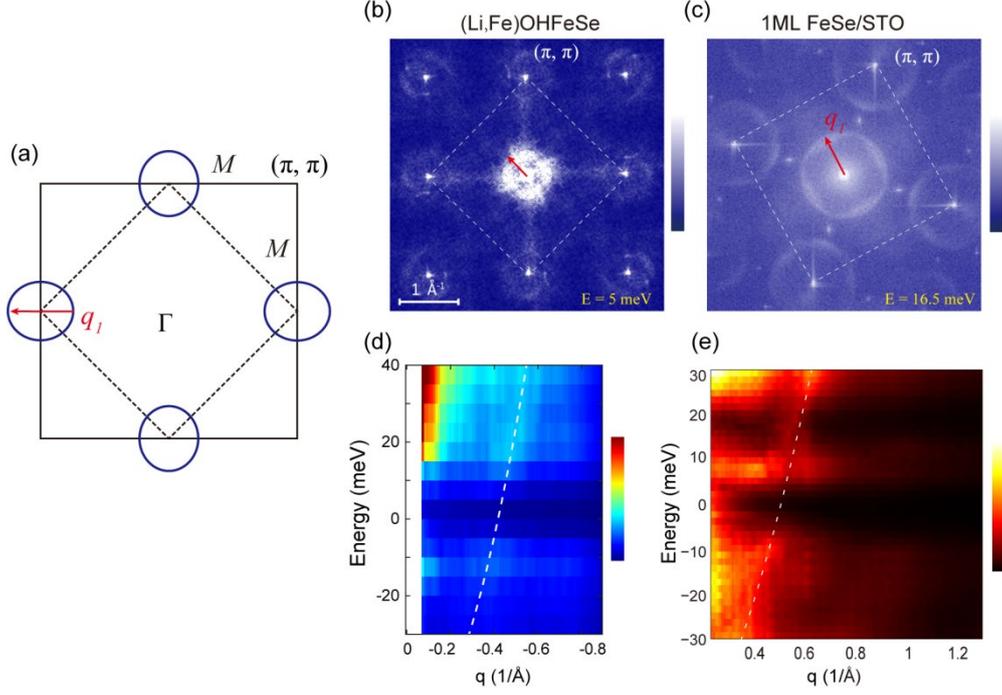
Fig. S2. (a) Schematic of the (unfolded) Brillouin zone (BZ) and Fermi surface of (Li,Fe)OHFeSe and single-layer FeSe/SrTiO$_3$(001). (b,c) The representative QPI pattern (FFT image) of (Li,Fe)OHFeSe and 1ML FeSe/SrTiO$_3$(001), measured at E= 5 meV and E = 16.5 meV (respectively). (d,e) The Q-space dispersion of the electron pocket of (Li,Fe)OHFeSe and 1ML FeSe/SrTiO$_3$(001), respectively. Dashed curves are parabolic fittings using $E = \frac{E_b}{q_F^2} q^2 - E_b$, which yield E_b = 50 meV, q_F = 0.35 Å^{-1} for (Li,Fe)OHFeSe, and E_b = 60 meV, q_F = 0.40 Å^{-1} for 1ML FeSe/SrTiO$_3$.

I- 2. Calculation of pinning force through the spatial variation of pinning energy

As illustrate in Fig. 3a, the pinning force f_p can be calculated through the spatial gradient of U_{pin} when the pinned vortex is forced to leave the pinning site (defect site). We calculated the U_{pin} difference between a pinned vortex measure at 7T and 6T, as shown in Fig. S3. The U_{pin} can be calculated by the similar method shown above, except that here the LDOS distribution is no longer isotropic (since the vortex is shifted away from the defect). Therefore, we used the dI/dV maps taken at various energies to do the spatial integration of LDOS, as shown in Fig. S3 below. The absolute value of LDOS is also calibrated in the similar way shown above. To increase the accuracy of the results, considering the superconducting DOS has particle-hole symmetry, the dI/dV was symmetrized with respect to zero-bias before integration.
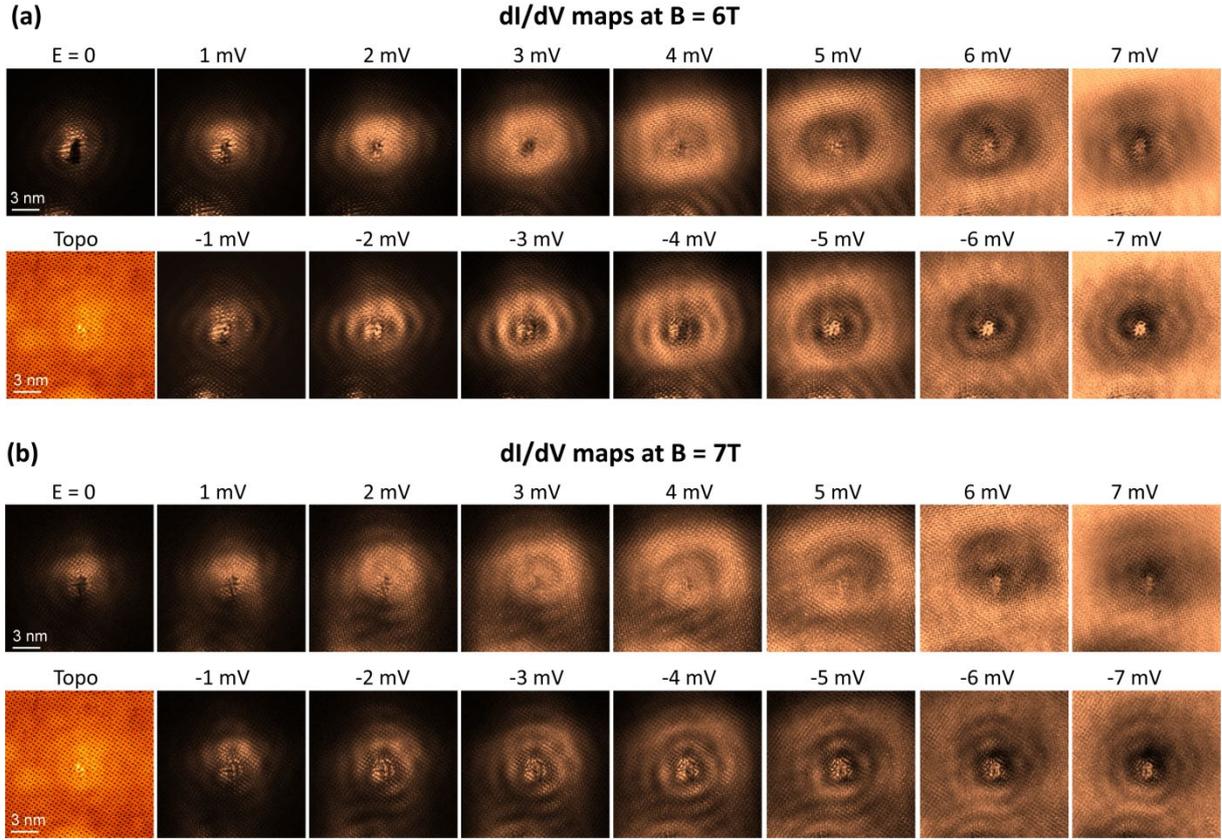
Fig. S3 (a) dI/dV maps of the pinned vortex taken at different energy, under B = 6T (setpoint: V_b = 10mV, I = 60pA, T_{eff} = 160mK). (b) dI/dV maps of the pinned vortex taken at different energy, under B = 7T (setpoint: V_b = 10mV, I = 60pA, T_{eff} = 160mK).

Part II: Microscopic modeling of the vortex CdGM state hybridized with the impurity state.

II -1. Model and method

The SC system under our investigation consists of a local impurity and a vortex, which are bound to each other. We start from normal state electrons with attractive interaction induced by electron phonon interaction. The BCS-reduced Hamiltonian in two-dimensions (2D) reads as $H_{BCS} = \sum_{k\sigma} \varepsilon_{k\sigma} c_{k\sigma}^\dagger c_{k\sigma} - (U/2) \sum_{k,k',\sigma,\sigma'} c_{k',\sigma}^\dagger c_{-k',-\sigma}^\dagger c_{-k,-\sigma}, c_{k,\sigma}$, where $\varepsilon_{k\sigma} = k^2/2m - \mu$ with m being the electron mass and μ the chemical potential of the normal state. At mean-field level and in the region away from the impurity and vortex, a uniform order parameter Δ_0 can be formed, leading to the conventional self-consistent equation for s-wave superconductors (SCs), i.e., $1 = (U/2) \sum_k 1/\sqrt{\varepsilon_{k\sigma}^2 + \Delta_0^2}$. Whereas, near the impurity and vortex, the spatial variation and the phase winding of the order parameter should be considered. The impurity its coupling to the SC also needs to be considered. Thus, the system is described by the quantum impurity model, $H = H_{SC} + H_{imp} + H_{hyb}$, where H_{SC} is the mean-field BCS Hamiltonian with spatially varying order parameter, i.e.,

$$H_{\mathrm{SC}} = \sum_{\sigma} \int d\mathbf{r} \left[-\frac{\hbar^2}{2m} \nabla^2 - \mu \right] c_{\mathbf{r}\sigma}^{\dagger} c_{\mathbf{r}\sigma} + \int d\mathbf{r} [\Delta(\mathbf{r}) c_{\mathbf{r}\uparrow}^{\dagger} c_{\mathbf{r}\downarrow}^{\dagger} + h.c.], \quad (1)$$

To incorporate the effect of a magnetic flux in the SC at $\mathbf{r} = 0$, we let $\Delta(\mathbf{r}) = \Delta(r) e^{i\nu\theta}$, where the radial dependence $\Delta(r) = \Delta_0 r / \sqrt{r^2 + \xi^2}$ is assumed (37), with ξ being the SC coherent length at the vortex, and ν an integer winding number. Clearly, $\Delta(r)$ vanishes at the origin $\mathbf{r} = 0$ and reaches Δ_0 for $r \gg \xi$. Meanwhile, the phase of the pairing potential goes from 0 to $2\pi\nu$ around $\mathbf{r} = 0$ with θ going from 0 to. In the following, we consider the case where the vortex carries one flux quantum, i.e., $\nu = 1$ is assumed. Here, the uniform order parameter Δ_0 and ξ are treated as parameters that are self-consistently determined in mean-field level.

Here, we consider the normal s-wave superconductor. It will be clear in the following that the shifting behavior of the CdGM modes remains qualitatively the same for other pairing symmetries, such as the p+ip pairing. Moreover, the shifting behavior of the CdGM modes does not rely much on whether the impurity is magnetic or non-magnetic. Thus, we consider a non-magnetic quantum impurity model described by

$$H_{\mathrm{imp}} = \sum_{\sigma} \epsilon_d d_{\sigma}^{\dagger} d_{\sigma}, \quad (2)$$

where $d_{\sigma}^{\dagger}(d_{\sigma})$ is the creation (annihilation) operator of the local impurity state with spin σ. Furthermore, the hybridization between the impurity and the electrons of the SC state is given by

$$H_{\mathrm{hyb}} = \sum_{\sigma} \int d\mathbf{r} [V_0(\mathbf{r}) d_{\sigma}^{\dagger} c_{\mathbf{r}\sigma} + h.c.], \quad (3)$$

where $V_0(\mathbf{r})$ is the scattering strength between the electrons in SC and the impurity, which usually takes the following form:

$$V_0(\mathbf{r}) = V_0 \frac{1}{\sqrt{\pi} r_0} e^{-(r/r_0)^2}, \quad (4)$$

where r_0 is the decaying length.

The Eqs. (1)-(3) above constitute a non-interacting Anderson-type quantum impurity model in a s-wave superconductor along with a magnetic vortex. The vortex center is located at the impurity position $\mathbf{r} = 0$ due to the pinning effect. It is also important to note that, the impurity in (LiFe)OHFeSe has a dumbbell shape that is of p-wave anisotropy (25). This brings about anisotropic scattering of the electrons in the SC. Thus, we further consider an anisotropic potential seen by the electrons, which is described by:

$$H_{\mathrm{ani}} = \sum_{\sigma} \int d\mathbf{r} V_1(\mathbf{r}) c_{\mathbf{r}\sigma}^{\dagger} c_{\mathbf{r}\sigma}, \quad (5)$$

where $V_1(\mathbf{r}) = 4V_1 \cos^2(\theta/2) e^{-(r/r_0)^2} / (\sqrt{\pi} r_0)$ is the strength of the p-wave scattering potential seen by the electrons around the impurity, and θ is the polar angle of $\mathbf{r}$. V_1 generates anisotropy, yet its value is dominated by the isotropic component V_0 in the experimental case. It is straightforward to include higher order scattering component in Eq.(5), however the shifting behavior of the CdGM mode remains qualitatively the same.

For the vortex-free case with $\nu = 0$, the SC Hamiltonian H_{SC} can be conveniently diagonalized by Bogoliubov transformation,

$$\gamma_n = \int d\mathbf{r} \sum_\sigma [u_{n\sigma}^*(\mathbf{r})c_{\mathbf{r}\sigma} + v_{n\sigma}^*(\mathbf{r})c_{\mathbf{r}\sigma}^\dagger],$$

$$\gamma_n^\dagger = \int d\mathbf{r} \sum_\sigma [u_{n\sigma}(\mathbf{r})c_{\mathbf{r}\sigma}^\dagger + v_{n\sigma}(\mathbf{r})c_{\mathbf{r}\sigma}], \tag{6}$$

where $\gamma_n^\dagger (\gamma_n)$ is the creation (annihilation) operator of the Bogoliubov quasi-particles. The Bogoliubov-de Gennes (BdG) equation leads to the eigenvalues E_n in the diagonal basis $\Phi_n(\mathbf{r}) = [u_{n\uparrow}(\mathbf{r}), u_{n\downarrow}(\mathbf{r}), v_{n\downarrow}(\mathbf{r}), -v_{n\uparrow}(\mathbf{r})]^T$, i.e.,

$$h_0(\mathbf{r})\Phi_n(\mathbf{r}) = E_n\Phi_n(\mathbf{r}), \tag{7}$$

where $h_0(\mathbf{r})$ is the single-particle Hamiltonian of the SC, i.e.,

$$h_0(\mathbf{r}) = \begin{bmatrix} -\dfrac{\hbar^2}{2m}\nabla^2 - \mu & 0 & \Delta(\mathbf{r}) & 0 \\ 0 & -\dfrac{\hbar^2}{2m}\nabla^2 - \mu & 0 & \Delta(\mathbf{r}) \\ \Delta^*(\mathbf{r}) & 0 & \dfrac{\hbar^2}{2m}\nabla^2 + \mu & 0 \\ 0 & \Delta^*(\mathbf{r}) & 0 & \dfrac{\hbar^2}{2m}\nabla^2 + \mu \end{bmatrix}, \tag{8}$$

In the presence of a vortex, $\nu = 1$, we make a gauge transformation $\Phi_n(\mathbf{r}) \to \tilde{\Phi}_n(\mathbf{r}) = e^{-i\nu\theta\tau_z/2}\Phi_n(\mathbf{r})$ where τ_z is the Pauli matrix in the Nambu space. Under the gauge transformation, the phase of the pairing potential is effectively removed, i.e., $\Delta(\mathbf{r}) \to \tilde{\Delta}(\mathbf{r}) = e^{-i\nu\theta}\Delta(\mathbf{r}) = \Delta(r)$. Thus, the transformation in terms of the basis reads as, $\Phi_n(\mathbf{r}) = e^{i\nu\theta\tau_z/2}\tilde{\Phi}_n(\mathbf{r}) = e^{i\nu\theta\tau_z/2}[u_{n\uparrow}(\mathbf{r}), u_{n\downarrow}(\mathbf{r}), v_{n\downarrow}(\mathbf{r}), -v_{n\uparrow}(\mathbf{r})]^T$. Then, we expand the wave function to the orbital angular momentum (OAM) space via $\Phi_n(\mathbf{r}) = \Sigma_m e^{-im\theta}\Phi_{nm}(r)$, where

$$\Phi_{nm}(r, \theta) = \int_0^{2\pi} d\theta \, \Phi_n(\mathbf{r}) = [u_{n,m+\nu/2\uparrow}(r), u_{n,m+\nu/2\downarrow}(r), v_{n,m-\nu/2\downarrow}(r), -v_{n,m-\nu/2\uparrow}(r)]^T.$$

(9)

Furthermore, to accurately solve the BdG equation, we expand the radial functions $u_{nm\sigma}(r)$, $v_{nm\sigma}(r)$ in the complete basis of Bessel functions, i.e.,

$$u_{nm\sigma}(r) = \sum_j u_{nmj\sigma}\phi_{mj}(r),$$

$$v_{nm\sigma}(r) = \sum_j v_{nmj\sigma}\phi_{mj}(r), \tag{10}$$

where

$$\phi_{mj}(r) = \frac{\sqrt{2}}{RJ_{m+1}(\beta_{mj})} J_m\left(\beta_{mj}\frac{r}{R}\right). \qquad (11)$$

$J_m(r)$ is the m-th order Bessel function defined in a disc of radius R, and β_{mj} is the j-th root of $J_m(r)$. The basis clearly satisfies the orthogonality, $\int_0^R dr\, r\phi^*_{mj'}(r)\phi_{mj}(r) = \delta_{jj'}$. Under the above basis, the BdG equation is finally cast into:

$$\begin{bmatrix} T_{m+\nu/2} & 0 & \Delta_{m+\nu/2,m-\nu/2} & 0 \\ 0 & T_{m+\nu/2} & 0 & \Delta_{m+\nu/2,m-\nu/2} \\ \Delta^t_{m+\nu/2,m-\nu/2} & 0 & -T_{m-\nu/2} & 0 \\ 0 & \Delta^t_{m+\nu/2,m-\nu/2} & 0 & -T_{m-\nu/2} \end{bmatrix}\begin{bmatrix} u_{nj,m+\nu/2\uparrow} \\ u_{nj,m+\nu/2\downarrow} \\ v_{nj,m-\nu/2\downarrow} \\ -v_{nj,m-\nu/2\uparrow} \end{bmatrix} = E_n^m \begin{bmatrix} u_{nj,m+\nu/2\uparrow} \\ u_{nj,m+\nu/2\downarrow} \\ v_{nj,m-\nu/2\downarrow} \\ -v_{nj,m-\nu/2\uparrow} \end{bmatrix},$$

(12)

where T_m and $\Delta_{m+\nu/2,m-\nu/2}$ are matrices in the Bessel function basis with the entries:

$$(T_m)_{ij} = -\left[\frac{1}{2m}\left(\frac{\beta_{mj}}{R}\right)^2 + \mu\right]\delta_{ij},$$

(13)

$$(\Delta_{mn})_{ij} = \int_0^R dr\, r\Delta(r)\phi_{mi}(r)\phi_{nj}(r).$$

The above transformation to the Nambu-OAM-Bessel basis can be written compactly in the second quantized form, namely, the original electron operators are transformed to the Bogoliubov quasiparticle operators via,

$$\gamma_{nm}^\dagger = \frac{1}{2\pi}\sum_\sigma \int d\mathbf{r}\, e^{im\theta}[u_{n,m+\nu/2,\sigma}(r)e^{i\nu\theta/2}c_{\mathbf{r}\sigma}^\dagger + v_{n,m-\nu/2,\sigma}(r)e^{-i\nu\theta/2}c_{\mathbf{r}\sigma}], \quad (14)$$

and

$$c_{\mathbf{r}\sigma} = \sum_{nm}[e^{im\theta}u_{n,m+\nu/2,\sigma}e^{i\nu\theta/2}\gamma_{nm} + e^{-im\theta}v_{n,m-\nu/2,\sigma}e^{i\nu\theta/2}\gamma_{nm}^\dagger]. \qquad (15)$$

By firstly turning off the coupling to the impurity, we can readily obtain the OAM-resolved energy spectrum of the SC with a vortex by diagonalization of the Hamiltonian in Eq. (12). As shown in Fig. S4, the in-gap states in Fig. S4 clearly demonstrate the existence of CdGM modes carrying different OAM quantum numbers, which are half integers $m = l + \nu/2$ with integer $l \in Z$. The CdGM modes with different OAM m have different energies, which are more and more away from zero energy with increasing $|m|$.
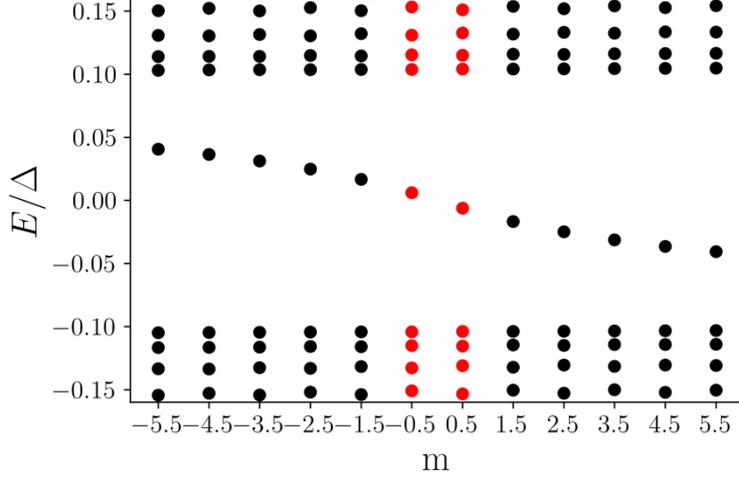
Fig. S4. The OAM-resolved energy spectrum with *m* from -11/2 to 11/2. The red dots highlight the spectra with the OAM *m*= ±1/2.

II -2. The effective coupling between the CdGM and the quantum impurity.

Using Eq. (15) above, the hybridization term in Eq. (3) can be mapped to

$$H_{\text{hyb}} = 2\pi \sum_{n\sigma} \int d\,rr V(r) d_\sigma^\dagger [u_{n0\sigma}(r)\gamma_{n,-1/2} + v_{n0\sigma}^*(r)\gamma_{n,1/2}^\dagger] + h.c. \quad (16)$$

Cleary Eq. (16) describes the coupling between the quantum impurity and the Bogoliubov quasi-particles with the OAM $m = \pm 1/2$, where we have focused on the case $\nu = 1$. The Bogoliubov quasi-particles that are coupled to the quantum impurity are marked by red in the energy spectrum as shown in Fig. S4. It is clear from Eq.(16) that, except for the above-gap bulk states, the in-gap states that are effectively coupled to the impurity only involves the lowest energy CdGM modes ($n = 0$) with the OAM $m = \pm 1/2$. From Eq. (16), their effective coupling can be read off as:

$$H_{\text{imp}-\text{CdGM}} = 2\pi\alpha \sum_{\sigma} \int d\,rr V_0(r) [u_{00\sigma}(r)d_\sigma^\dagger \gamma_{0,-1/2} + v_{00\sigma}^*(r)\gamma_{0,1/2}^\dagger d_\sigma] + h.c., \quad (17)$$

where $V_0(r) = V_0 e^{-(r/r_0)^2}/(\sqrt{\pi}\,r_0)$. The mixing term above will inevitably shift the energy level of both the lowest CdGM mode and the quantum impurity state. In order to trace the effect of the impurity-CdGM coupling, we intentionally introduce a controlling factor α with $\alpha \in [0, 1]$ in front of Eq. (17). For $\alpha = 0$, one artificially turns off the impurity-CdGM coupling, while $\alpha = 1$ reproduces the realistic case with the full coupling.

In terms of the impurity scattering term, we firstly consider the isotropic and short-range case by taking $V_1 = 0$ and $r_0 \to 0$. In this case, the Gaussian function in $V_0(r)$ approaches the delta-function $\delta(\mathbf{r})$. We numerically solve the Eq. (2), Eq.(12) and Eq. (16) in the Nambu-OAM-Bessel basis introduced above. In our calculation, we introduce a cutoff $N = 100$ in terms of the Bessel basis function, which is sufficient as we have numerically confirmed that the results are saturated and remain unchanged for even larger N.

Fig. S5(a)(b) shows the evolution of the energy levels of the in-gap states with increasing the broadening function $\Gamma = \pi \rho_0 V_0^2$, where ρ_0 is the density of states (DOS) of the normal state. As shown in Fig. S5, the behavior of the in-gap states with increasing Γ strongly depends on the relative energies of the impurity state and the CdGM mode at zero coupling $V_0 = 0$. From Fig. S5(a) where $\epsilon_d < |E_{\text{CdGM},0}|$, we find that when the effective coupling between the two states is turned off with $\alpha = 0$, the impurity level and the lowest CdGM mode (with OAM $m = \pm 1/2$) crosses with each other with increasing Γ (the dashed curves in Fig. S5(a)). Hence, under the full coupling with $\alpha = 1$, the two states strongly hybridize with each other, as shown by Fig. S5(a). This is further verified by the calculated ratio of the wave function amplitude of the two states, as shown by Fig. S5(c). However, in Fig. S5(b) where $\epsilon_d > |E_{\text{CdGM},0}|$, the two states do not cross with each other at $\alpha = 0$, as shown by the dashed curves. Thus, we do not observe a strong mixing of the two states. Instead, the coupling between the two states generates the shifting of the CdGM mode. Specifically, the impurity state at the electron (hole) side is pushed to higher (lower) energies while the $m = 1/2$ ($m = -1/2$) CdGM mode is pushed towards lower (higher) energies. Interestingly, the $m = 1/2$ and the $m = -1/2$ CdGM modes cross with each other at zero energy at a critical Γ_c, as shown in Fig. S5(b).

The evolution of the impurity state (on the electron side) and the $m = 1/2$ CdGM mode is shown in Fig. S5(d), with a fixed Γ and an increasing α. It is clearly shown that the impurity-CdGM hybridization has a "repulsion effect", which pushes the two states away from each other in energies. As will be clear in the following, this "repulsion effect" can well account for our experiments at the quantitative level.

It should now be clear that, since it is the coupling with the impurity that drives the shift of the CdGM state, and the coupling remains qualitatively unchanged for other pairing symmetries, e.g., the p+ip SC, the shifting behavior of the CdGM mode should be insensitive to the SC pairing symmetries. This further supports our starting point in Eq.(1).
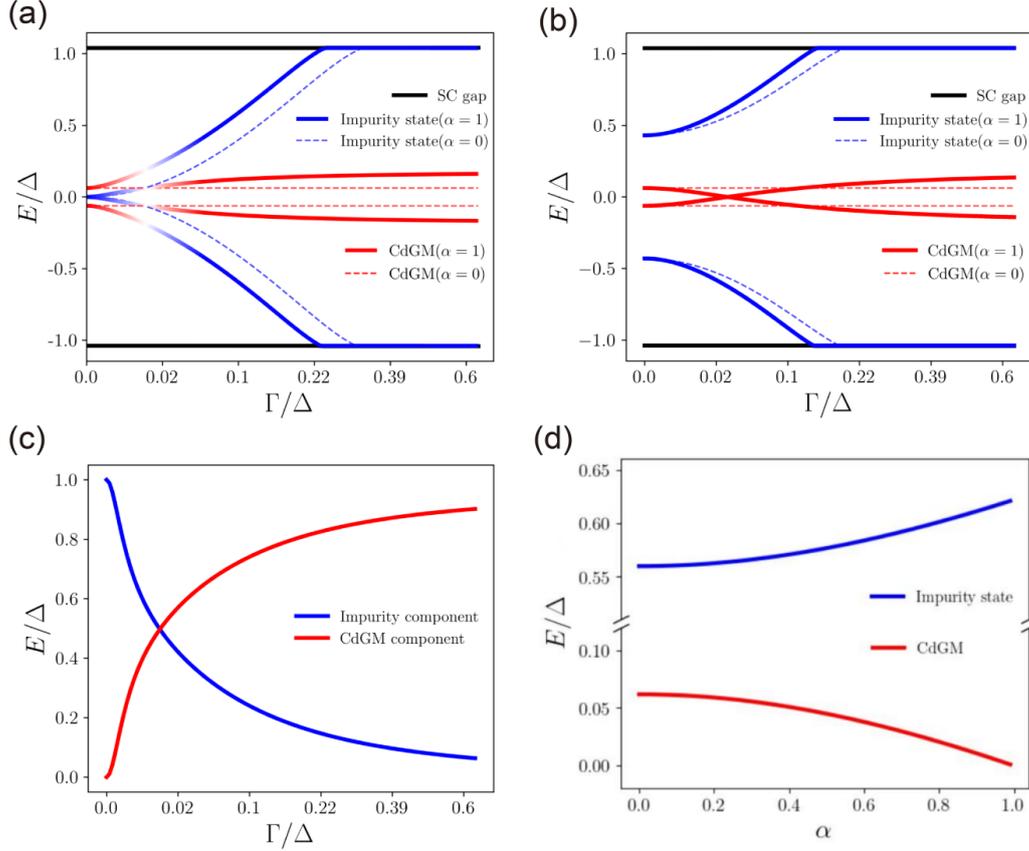
Fig. S5. The in-gap states calculated for the isotropic scattering $V_1 = 0$. (a,b) The in-gap states as a function of the broadening function Γ. The solid and dashed curve show the results for $\alpha = 1$ and 0, respectively. (c) The calculated ratio of the wave function amplitude between the impurity and the CdGM state as a function Γ. (d) The evolution of the impurity state (on the electron side) and the $m = 1/2$ CdGM state with varying α from 0 to 1. Γ is set to the critical value Γ_c where the $m = 1/2$ and $m = -1/2$ CdGM modes cross with each other in (b). $\epsilon_d = 0$ is used in (a,c) and $\epsilon_d = 0.043$ in (b,d).

II -3. Self-consistent determination of the local pairing function around the vortex core.

In real space, the shift of the CdGM state is manifested by the localization around the vortex center. We calculate the spatial distribution of the two lowest CdGM states for different Γ. As shown by the Fig. S6(a),(b), the CdGM states become much more localized for the pinned vortex case. Thus, more states are squeezed towards the vortex center $r = 0$. Consequently, the local gap function $\Delta(r)$ around the vortex center is expected to be effectively enhanced.

The gap function $\Delta(r)$ around a free vortex should, in principle, be self-consistently determined. According to previous studies, e.g., Ref. (*36*), a satisfactory description of the gap function can take the form as $\Delta(r) = \Delta_0 r / \sqrt{r^2 + \xi^2}$. It should be noted that the shape of the gap profile is known to affect only slightly the quasi-particle energies; it does not change the key features of the vortex core states which are mainly controlled by the vortex topology. Therefore, the adopted function form of $\Delta(r)$ is expected to closely reproduce the true core

spectrum and the corresponding eigenstates, for both the free vortex and the pinned vortex cases.

When the vortex is pinned by the defect, the gap functions $\Delta(r)$ will be quantitatively modified (without affecting the vortex topology). Since Δ_0 is the gap away from the vortex, its value remains unchanged. Whereas, the local coherent length ξ in $\Delta(r)$ can be modified. In order to investigate how the local pairing is changed by the defect, we treat ξ as a variational parameter in the SC order parameter, and self-consistently determine its value at the mean-field level. Specifically, we calculate the total energy of the whole system,

$$E_{\text{sys}} = E_{\text{CdGM}} + E_{\text{imp}} + E_{\text{SC}} + \frac{\Delta_0{}^2}{U},$$

where U is the attractive interaction between electrons induced by the electron-phonon coupling, E_{SC} is the mean-field energy of all the Bogoliubov quasi-particles in the bulk continuum below the Fermi level, and E_{CdGM} and E_{imp} are the energy of the in-gap CdGM states and the impurity states, respectively, which are dependent on $\Delta(r)$ and thus on ξ. The SC gap away from the vortex Δ_0 is determined by the conventional gap equation $1 = \frac{1}{2} U \sum_k \frac{1}{\xi_k}$, where $\xi_k = \sqrt{(\frac{k^2}{2m} - \mu)^2 + \Delta_0^2}$. Through minimizing E_{sys}, we are able to determine ξ for different impurity coupling V_0 (and fixed U). The results are shown by Fig. 4(e) of the main text, where we observe that ξ decreases with increasing V_0 or Γ. Hence, compared to the free vortex case, the local pairing potential is effective enhanced when an impurity is in presence.

We also plot the calculated LDOS at the vortex center for different parameters in Fig. S6(c),(d), with taking into account the contribution from all the CdGM states, the impurity state and the above-gap continuum. For a larger broadening factor, we observe from Fig. S6(d) that the SC gap (the black curve) is effectively obscured by the vortex due to the in-gap CdGM states (the blue curve), which is however enhanced when one further considers the pinning effect of the impurity (the red curve). For a smaller broadening factor, the in-gap peaks are more clearly shown, as displayed by Fig. S6(c). We note Fig. S6(c) and (d) are in qualitative agreement from the experimental data in Fig. 1(h) and Fig. 2(c) of the main text.
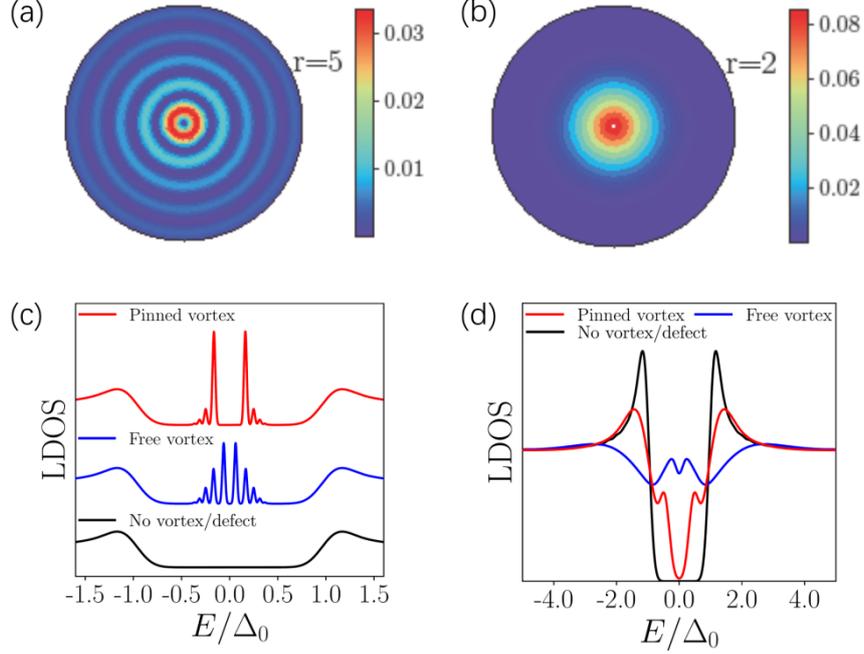
Fig. S6. The spatial distribution of the lowest CdGM mode in a free vortex (a) and impurity pinned vortex (b). (c) and (d) The LDOS calculated for (i) the clean SC, (ii) the free vortex (at vortex center), and (iii) the pinned vortex case (at vortex center), with taking into account the contribution from all the CdGM states, the impurity states, and the above-gap continuum. The delta function encountered in the calculations are approximated by Gaussian function with a broadening factor b. (c) and (d) show the results for $b = 0.002$ and $b = 0.02$, respectively. The larger broadening factor in (d) observe the discrete spectrum in (c).

II -4. Comparison with experiments.

We now consider the more realistic case where the impurity scattering has anisotropy with nonzero V_1. The anisotropic scattering component V_1 introduces a new hybridization term in the Nambu-OAM-Bessel basis, i.e.,

$$H_1 = \sum_{\sigma} \int drr V_1(r) \sum_{mn} [u^*_{m0\sigma}(r) u_{n1\sigma}(r) - v^*_{m,-1\sigma}(r) v_{n0\sigma}(r)] \gamma^{\dagger}_{m,-1/2} \gamma_{n1/2} + h.c., \quad (18)$$

where $V_1(\mathbf{r}) = 4V_1 \cos^2(\theta/2) e^{-(r/r_0)^2}/(\sqrt{\pi} r_0)$. Clearly, Eq. (18) introduces a direct coupling between the two lowest CdGM modes with $m = 1/2$ and $m = -1/2$. The energy spectra of the in-gap states are calculated and shown in Fig. S7(a), (b) with taking into account the nonzero V_1. It is found that the direct coupling between the CdGM modes with $m = 1/2$ and $m = -1/2$ always gaps out the gapless crossing point at Γ_c. The gapless point is sensitive to V_1, as the latter breaks the OAM conservation. The gap value with increasing V_1 is shown in Fig. S7(b). As shown, the gap becomes quite significant even for the case with a relatively small anisotropy, i.e., $V_1 < V_0$.
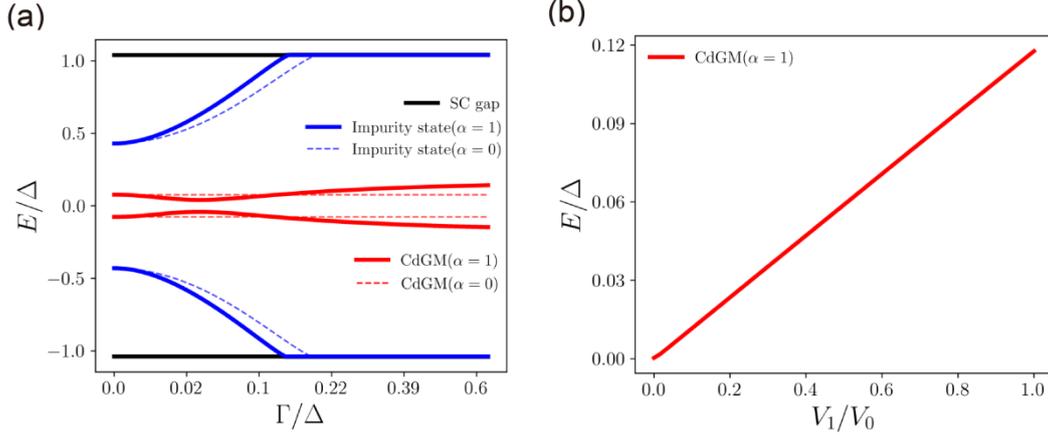
Fig. S7. (a) The in-gap states with anisotropic scattering. The solid and dashed data are results for $\alpha = 1$ and 0 respectively. (b) The energy gap at Γ_c caused by the anisotropy as a function of V_1/V_0.

Finally, to make quantitative comparison with our experiments, we now consider the impurity scattering of a finite range, i.e., $r_0 \neq 0$ in Eq. (4). $V_0(r)$ now decays with the distance r from the impurity (vortex) center. In our experiments, the STM tip is gradually moved along a line-cut towards and then away from the impurity center. The distance between the tip and the impurity center is denoted by d. Since STM measures the local DOS at the tip site, we can use the scattering strength at $r = d$, i.e., $V_0(d)$, to simulate the local quantity measured by our experiments. With tuning the position of STM tip, $V_0(d)$ is accordingly varied, leading to a continuous evolution of the in-gap states in our calculations. The calculated results with tuning d are shown in Fig. S8(a), which are compared to the experimental data marked by stars. Here, we only plot the lowest CdGM mode and the impurity state for clarity. A more complete comparison between our calculations and experiments is illustrated in Fig. S8(b) and (c). As shown, our calculation successfully accounts for the shifting behavior of the CdGM modes at quantitative level. Our calculations also predict a shifting of the impurity state to higher energy until it reaches the SC gap edge. Corresponding signatures can be found in Fig. S8(c), which is however obscured by the other in-gap CdGM states. This could be an interesting signature for further exploration.
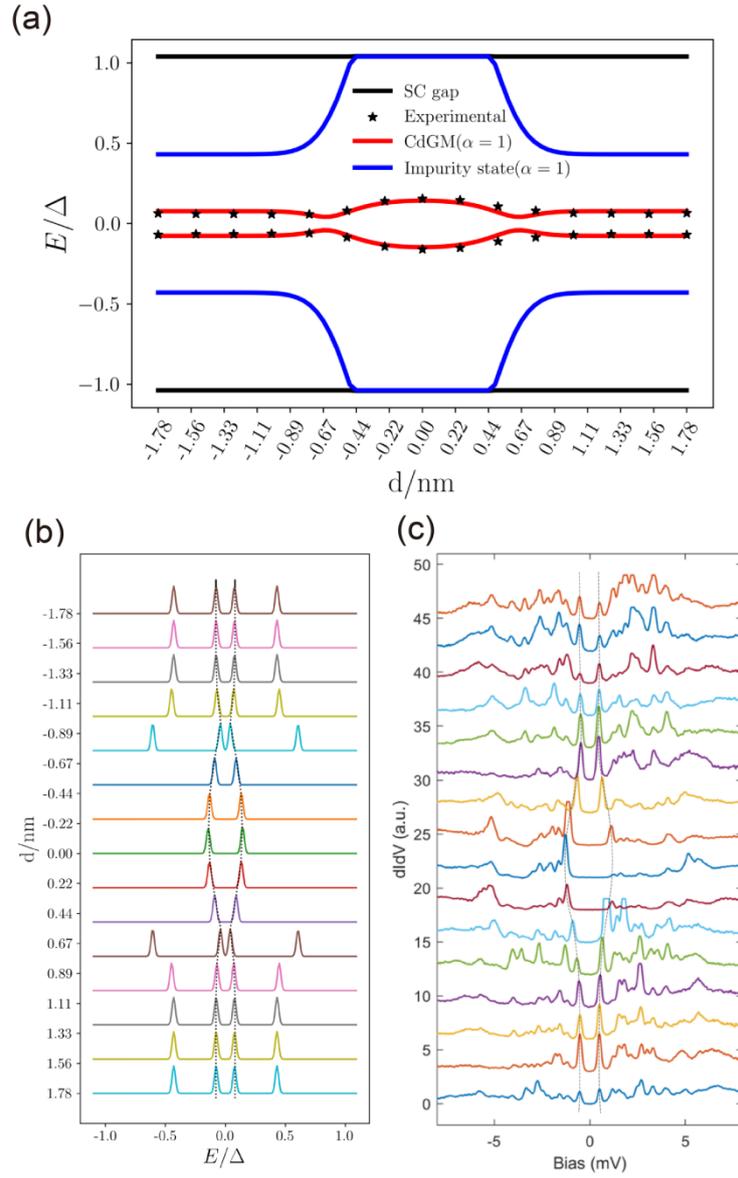
Fig. S8. The comparison between the numerical simulation and the STM data in experiments. The dashed curves in (b) and (c) indicate the evolution of the lowest CdGM state with moving the STM tip. The parameters used have been illustrated in the main text.